Simulation of overflow nappe impingement jets

Luis G. Castillo, José M. Carrillo and Álvaro Sordo-Ward

ABSTRACT

Rectangular jets constitute one of the energy dissipation methods in the overtopping of dams. The high turbulence and aeration phenomena that appear in falling jets and dissipation basins make it difficult to carry out studies based only on classical methodologies. There are studies modelling spillways with computational fluid dynamics which produces accurate results. However, the study of overflow nappe impingement jets has not been sufficiently examined. Simulations of free air–water overflow weirs are scarce, and require small mesh sizes and a high computational effort. This work seeks to address such simulation. Results obtained with ANSYS CFX are compared with laboratory measurements and empirical formulae. To identify the level of reliability of computed parameters, validation of air entrainment and velocity along free falling jets, thickness and break-up of jets, and pressures on the bottom of the plunge pool, are carried out by using a two-fluid model, turbulence models and mesh-size analysis. Good agreement is obtained with experimental and theoretical data. The results show that air entrainment in the jet is highly sensitive to the mesh size, while the choice of the turbulence model seems to have only a relative effect on the stagnation point.

Key words | air entrainment jet, computational fluid dynamics (CFD), energy dissipation, impingement jets, plunge pools, turbulence models

Luis G. Castillo (corresponding author)
José M. Carrillo
Álvaro Sordo-Ward
Civil Engineering Department,
Universidad Politécnica de Cartagena,
UPCT,
Paseo Alfonso XIII,
52 – 30203 Cartagena,
Spain
E-mail: *luis.castillo@upct.es*

NOMENCLATURE

a, b	parameters of the mean dynamic pressure coefficient
ADV	acoustic Doppler velocimeter
b_{distrib}	width of the influence point (distance between the upstream and downstream points in which $p = H_m/2$)
b_j	impingement jet width in the transversal direction
B_g	jet thickness by gravity conditions
B_i	jet thickness at issuance conditions
B_j	jet thickness at impingement conditions
BSL	baseline Reynolds stress turbulence model
C_d	discharge coefficient
C_p	mean dynamic pressure coefficient
$C_{\varepsilon 1}$, C_μ	coefficients of the k-ε turbulence model
$C_{\varepsilon 1RNG}$, $C_{\mu RNG}$	coefficients of the RNG turbulence model
CFD	computational fluid dynamics
D_j	diameter of circular jet at impingement condition
F_D	square Froude number in the water cushion
F_i	Froude number at the issuance conditions
F_1	blending function
g	gravity acceleration
h	energy head over the weir
h_0	height between upstream water level and issuance conditions level
H	height between upstream water level and downstream water level
H_m	head mean registered at stagnation point of the plunge pool bottom
IC	initial conditions
k	turbulent kinetic energy
K	fit coefficient in the parametric methodology

doi: 10.2166/hydro.2014.109

K_3	coefficient for the mean dynamic pressure coefficient in the longitudinal direction considering x/x_{max} ratio
K_φ	turbulent parameter coefficient
L_b	jet break-up length
p	pressure
P	vertical distance from the weir to the bottom of the dissipation basin
P_k	turbulence production due to viscous forces
q	specific flow
r_α	volume fraction of α phase
RANS	Reynolds-averaged Navier–Stokes equations
RMS	root mean square velocity
RSM	Reynolds stress model
RNG	re-normalisation group analysis of the Navier–Stokes equations turbulence model
S_{ij}	mean strain-rate tensor
SST	shear-stress transport turbulence model
t	time
t_{Gi}	time during which the probe is in gas
T_u	turbulent intensity
T_u*	turbulent intensity at issuance conditions estimated for laboratory test cases
u_i'	turbulent velocity component
U	velocity vector
V_D	mean velocity in the water cushion
V_i	mean velocity at issuance conditions
$\overline{V_i'}$	RMS velocity at issuance conditions
Vj	mean velocity at impingement conditions
w'	streamwise turbulent velocity
x, y, z	coordinate directions
x^*, z^*	coordinates axis considering that the origin is in the weir crest
X_{imp}	horizontal distance from the weir to the stagnation point
x_{max}	maximum longitudinal distance extension of the zone that is influenced by the turbulent shear layer of the impacting jet
Y	water cushion depth
Y_u	water cushion depth under nappe
y_k	depth to disintegrate the jet central core in the water cushion

Greek letters

α	fluid phase
β	head loss coefficient
β_{RNG}	constant of the RNG turbulence model
δ	Kronecker delta function
ε	turbulence dissipation ratio
θ	impingement jet angle
μ	molecular viscosity
μ_t	eddy viscosity or turbulent viscosity
ξ	jet lateral spread distance by turbulence effect
ρ	flow density
$-\rho\overline{u_i'u_j'}$	Reynolds stress
φ	turbulence parameter in nappe flow case
ϕ'	parameter of the pressure distribution near the stagnation point
ω	turbulent frequency

INTRODUCTION

In recent years, the increasing magnitude of design floods has prompted re-evaluations of spillway capacity and operational scenarios for large dams throughout the world. Current capacity of many spillways is inadequate, raising the possibility that dams might be overtopped during extreme events. Creating additional spillway capacity is often expensive and sometimes technically infeasible and, in these cases, dam owners sometimes consider accepting overtopping as a planned operation during extreme events. This creates new loading scenarios for the dam and raises questions about erosion and scour downstream from the dam (Wahl *et al.* 2008).

Rectangular jet or nappe flow constitutes one of the energy dissipation methods in the overtopping of dams. In turbulent flow, the pressure fluctuations are the main mechanism in the incipient movement of the particles. The erodibility index relates the relative magnitude of the erosive capacity of water and relative resistance of the material (natural or artificial) to resist erosion (Annandale 2006). Another interesting approach to obtain the scour hole is that of the use of an adaptive neuro fuzzy inference system (Azamathulla *et al.* 2009). In order to obtain the right pool

depth, the designer needs to know the magnitude, frequency and extent of the dynamic pressures on the pool floor as a function of the jet characteristics.

Considerations

There are different empirical formulae to characterise the pressures at the stagnation point on the bottom of plunge pools. Due to the high difficulty in instrumenting prototypes, all of them were obtained using different scale models, with some being carried out by Moore (1943), Castillo (1989), Puertas (1994), Ervine *et al.* (1997), Bollaert & Schleiss (2003), Melo *et al.* (2005), Annandale (2006), Castillo *et al.* (2007), Federspiel (2011), Asadollahi *et al.* (2011), and Castillo & Carrillo (2011, 2012, 2013). In general empirical formulations, the pressure was considered as a function of the falling height, the depth on the plunge pool and the jet characteristics (thickness, shape, impingement velocity and turbulence).

The region of the flow where energy dissipation takes place may be divided in diverse steps: the spreading of the plunging jet (aeration and atomisation of the jet during the fall), the air entrainment and diffusion of the jet in the pool and, finally, the impact on the pool bottom. With the aim of designing considerations it is necessary to define both the issuance conditions and the impingement conditions.

The issuance conditions are located in the section with height $z = -h$ and downstream from the spillway structure, with z being the vertical component with origin in the crest weir, and h the energy head over the weir (Figure 1).

The impingement conditions are obtained in the jet section before the impact with the surface of the plunge pool. The mean velocity, V_j, and the impingement jet thickness, $B_j = B_g + 2\xi$, are defined, where B_g is the jet thickness by gravity conditions (which decreases due to the gravity effect) and ξ is the jet lateral spread distance by turbulence effects. Davies (1972) postulated that the lateral spread distance is approximately equal to the square root of the fall distance.

An additional important parameter is the jet break-up length, L_b. Beyond this distance, the jet is completely developed. It no longer contains a non-aerated core but

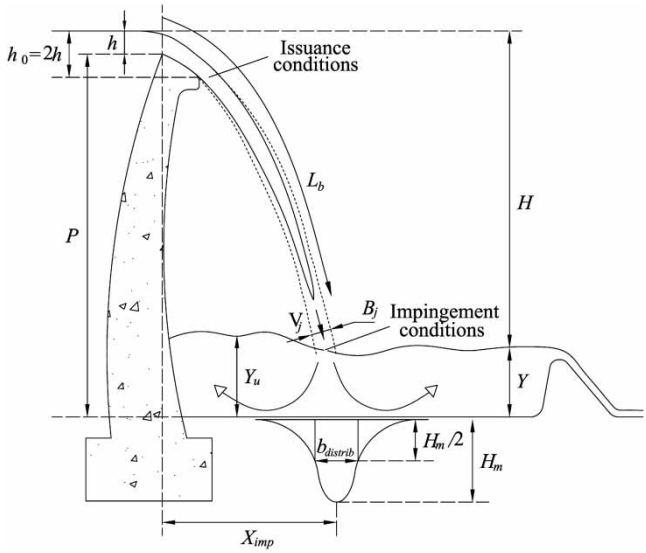

Figure 1 | Scheme of falling rectangular jets.

consists essentially of blobs of water that disintegrate into finer and finer drops. For flows smaller than $q = 0.25\ \mathrm{m^2/s}$ (laboratory test values), Horeni's formulae $L_b \sim 6q^{0.32}$ (cited by Ervine *et al.* 1997) seems to be correct (Castillo 2006).

The disintegration conditions of circular jets have been thoroughly examined, though mainly by Ervine *et al.* (1997). However, the case of rectangular jets has not been studied in sufficient depth. The only expression known for the rectangular jet break-up length is that proposed by Horeni (1956).

Previous studies carried out by the authors in this field analysed the applications of commercial computational fluid dynamics (CFD) codes to simulate overflow nappe impingement jets in a general way, where the type of mesh elements and scale effects were analysed (Castillo & Carrillo 2011, 2012, 2013). Continuing the research, this work is focused on the sensibility analysis of the mesh size and turbulence models, before carrying out a systematic study that considers specific flows and water cushions. New laboratory data (velocity, pressure and air entrainment rate) were obtained. All simulations were specifically performed for this work. ANSYS CFX was selected due to the accuracy tests of the authors in stagnation points, air entrainment in the jet, and its wide turbulence model gallery.

Numerical simulations

For the turbulent flow, CFD codes solve the differential Reynolds-averaged Navier–Stokes (RANS) equations of the phenomenon in the fluid domain, retaining the reference quantity in the three directions for each control volume identified. The equations for conservation of mass and momentum may be written as

$$\frac{\partial \rho}{\partial t} + \frac{\partial}{\partial x_j}(\rho U_j) = 0 \tag{1}$$

$$\frac{\partial \rho U_i}{\partial t} + \frac{\partial}{\partial x_j}(\rho U_i U_j) = -\frac{\partial p}{\partial x_i} + \frac{\partial}{\partial x_j}\left(2\mu S_{ij} - \rho\overline{u_i' u_j'}\right) \tag{2}$$

where i and j are indices, x_i represents the coordinate directions ($i = 1$ to 3 for x, y, z directions, respectively), ρ the flow density, t the time, U the velocity vector, p the pressure, u_i' presents the turbulent velocity in each direction ($i = 1$ to 3 for x, y, z directions, respectively), μ is the molecular viscosity, S_{ij} is the mean strain-rate tensor and $-\rho\overline{u_i' u_j'}$ is the Reynolds stress.

Eddy-viscosity turbulence models consider that such turbulence consists of small eddies which are continuously forming and dissipating, and in which the Reynolds stresses are assumed to be proportional to mean velocity gradients. The Reynolds stresses may be related to the mean velocity gradients and eddy viscosity by the gradient diffusion hypothesis:

$$-\rho\overline{u_i' u_j'} = \mu_t\left(\frac{\partial U_i}{\partial x_j} + \frac{\partial U_j}{\partial x_i}\right) - \frac{2}{3}\delta_{ij}\left(\rho k + \mu_t \frac{\partial U_k}{\partial x_k}\right) \tag{3}$$

with μ_t being the eddy viscosity or turbulent viscosity, $k = 1/2\overline{u_i' u_i'}$ the turbulent kinetic energy and δ the Kronecker delta function.

CFD simulations may be used by solving different fluid mechanical problems of significant interest in civil engineering, such as the stratification caused by salinity and temperature, pollutant transport (Chau & Jiang 2001, 2004), water quality (Wu & Chau 2006) or flows in natural rivers (Lai & Khan 2012).

In preparing this study, an extensive literature review of hydraulic dams was carried out. However, given that the CFD methodology is relatively recent there are few well documented references for free overflow spillways. For this reason, it is necessary to review CFD accuracy in similar typologies.

One literature review was carried out by Ho & Riddette (2010). Although there are many benefits of using CFD methodology, there are some limitations that do not allow researchers to perform feasible studies in the hydraulic dam field. Table 1 collects the simulation limitations related with free overflow spillways, based on diverse spillways analysis and the experience of different authors.

Studies of free overflow weirs are scarce and, those that are found do not specify or detail discussion related with turbulence models. Nevertheless, there are turbulence model studies in neighbouring fields that may help us in a first attempt to ascertain the jet behaviour.

Wilcox (2006), for example, analysed the free shear flow spreading rates of different types of jets using two-equation models: standard k-ε, re-normalisation group (RNG) k-ε and k-ω. The k-ω model was the closest to measurements, with results falling within the range of measured values (using the average values from the measured ranges, the average difference was 6%). The k-ε model predicted the plane jet spreading rate falling

Table 1 | Current limitations and suggestions for future research (Ho & Riddette 2010)

Limitation	Progress to date	Suggested further work
Air demand	Not attempted by authors.	Validation of air demand along chutes and behind free falling jet.
Thin jets and break-up of jets	Limited progress with single-fluid model at the jet core only. Requires a very fine mesh resolution.	Extend to two-fluid model to include air entrainment and jet break-up. Validate impact pressures against experimental data.
Fluctuating pressures at spillways	Observed results from RANS turbulence models with relatively coarse mesh. No validation to date.	Parametric study with mesh size and turbulence models to identify level of reliability of computed pressure.

within the range of measured values, while the average difference between computed and average measured spreading rates was 17%. The RNG k-ε model yielded larger differences, with an average of 36%.

Azis *et al.* (2008) studied plane and circular turbulent non-buoyant deeply submerged jets by using standard k-ε and RNG k-ε models. In both plane and circular turbulent jets, the k-ε scheme performed better in predicting the growth rate and the decay of the centreline longitudinal velocity, and slightly better than the RNG model in predicting longitudinal and vertical velocity profiles. However, the two schemes were unable to predict the kinetic energy, especially in the case of circular jets.

Guha *et al.* (2010) simulated the entrainment of surrounding air into high-speed water jets. Simulations accurately predicted the centreline velocity, pressure and volume fraction distributions, but under-predicted the velocity and over-predicted the volume fraction distribution near the jet edge. Since the near-edge region was predominately a sparse droplet flow region, the Eulerian models failed to capture the physics accurately.

Haun *et al.* (2011) performed two-dimensional numerical simulation of a broad-crested weir by using two CFD codes with different free surface algorithms and types of mesh. The standard k-ε turbulence model was considered. The deviation of the upstream water level from the physical model test was between 0.95 and 3.49%. Comparing each code, the deviations in the discharge coefficient were between 0.0 and 2.2%.

Balabel *et al.* (2011) performed numerical simulation on two-dimensional rocket nozzles by using six different turbulence models, and compared the static wall pressure and the shock position with experimental data. They found that the k-ω based shear-stress transport (SST) turbulence model exhibited the best overall agreement with the experimental measurements. However, the nozzle they simulated did not introduce secondary flow or induce oblique shock waves.

Mahmoud *et al.* (2012) used the standard k-ε model and Reynolds stress model (RSM) to solve the recirculation of turbulent co-flowing jets. They obtained close results to laboratory measurements for velocity with the two turbulence models. However, results were quite different for the temperature and the turbulent kinetic energy. For high Froude numbers, the difference between the temperature profile results obtained a maximum of 8%, while the k-ε model overestimated the normalised kinetic energy on the jet axis, though the difference between the results did not exceed 7%.

Rahimzadeh *et al.* (2012) simulated flow over circular spillways with different turbulence models (standard k-ε, RNG k-ε, realisable k-ε, standard k-ω, SST and RSM). They determined that the flow over the spillway had been reproduced with sufficient accuracy by all turbulence models, except the standard k-ε and the standard k-ω. The RSM turbulence model had the best agreement with experimental data among all the turbulence models.

Purpose

As a result of the increasing magnitude of design floods and the inaccurate capacity of many spillways in large dams throughout the world, the scour due to overtopping rectangular jets downstream of concrete dams is a point of great interest in the dam field.

Researches to date have been developed in the laboratory using scale models. The CFD programs allow researchers and designers to evaluate different effects with a smaller cost than that incurred building scale models. However, there are scarce references to numerical simulations of overtopping jets and their effects on the plunge pool.

As a result of the lack of numerical simulations in this field, this paper is focused on filling the gap between laboratory results and CFD simulations in overtopping rectangular jets. ANSYS CFX software (version 12.1) is used to analyse the pressure distribution on the bottom of the plunge pool, and velocities and air entrainment rates in the falling jet. Due to the variety of turbulence models, and in order to compare their effect over different parameters, three distinct two-equation turbulence models are examined. In addition to this, a RSM based on the ω-equation is used to solve the turbulence component velocities in the falling jet.

Knowing the parameters analysed, designers will be able to estimate the scour effects and the stability of the dam with a higher certainty.

LABORATORY EXPERIMENT

Turbulent jet experimental facility

The hydraulics laboratory at the Universidad Politécnica de Cartagena in Spain has a turbulent jet experimental facility in which the energy dissipation of turbulent rectangular jets is being studied. The mobile mechanism allows researchers to vary the discharge heights between 1.70 and 4.00 m and flows from 10 to 150 l/s. It has an inlet channel with a length of 4 m and width of 0.95 m, in which different dissipation systems have been located. The weir is a sharp crest with a width of 0.85 m and height of 0.37 m.

The plunge pool, in which different water cushions may be regulated, is a 1.60 m high and 1.05 m wide box made of methacrylate. Instantaneous pressure measurements were registered with piezoresistive transducers located on the plunge pool bottom, kinetic energy at the inlet channel with acoustic Doppler velocimeter (ADV) equipment, mean velocities and air entrainment rate in different sections of the falling jet with optical fibre instrumentation.

For the impingement jet width in the transversal direction, b_j, photographs were obtained from the downstream side. The width was measured by digitalising the resulting image.

The flow was measured with a V-notch weir, located downstream from the plunge pool. The discharge rate of the V-notch was tested with a velocity-area method using ADV equipment upstream from the weir. Differences between V-notch results and the velocity-area method were smaller than 5% of the current flow.

Experiments carried out in this study correspond to different falling heights H between 1.70 and 3.00 m, seven water cushion heights Y (from direct impact to 0.60 m) and seven specific flows q (from 0.020 to 0.064 m^2/s). Laboratory data cover a range of $0.60 \leq H/L_b \leq 2.02$. Almost 190 registers were obtained, with each one being of 7,200 points and with an acquisition rate of 20 samples per second.

Pressure transducers

With the aim of obtaining the instantaneous pressures, GE Druck model UNIK 5000 pressure transducers were used. The sensors were located on the bottom of the plunge pool, at the symmetry plane of the turbulent jet device and equally spaced at 5 cm intervals. These sensors have a pressure range between −200 and +800 mbar and a precision of ±0.04% of the full scale output. After carrying out a static calibration, the pressure precision of the transducers was ±0.01 water column metres. Instantaneous pressures were obtained by considering a frequency rate of 20 Hz and measurements of 360 s. In each measurement, seven sensors were used at the same time (one at the stagnation point, three upstream from the stagnation point, and three downstream).

Optical fibre equipment

To measure the mean velocity and the air entrainment at the falling jet, an RBI-instrumentation dual-tip probe optical phase-detection instrument was used. This equipment enables measurement in water up to 20 m/s flow velocity and the relative uncertainty concerning the void fraction is estimated at about 15% (Stutz & Reboud 1997a, b). The rise and fall of the probe signal corresponds, respectively, to the arrival and the departure of the gas phase at the tip of the sensor. The thresholding values were set to 1.0 and 2.5 V (Boes & Hager 1998).

The void fraction was defined as the ratio of the total time the probe is in gas (Σt_{Gi}) to the experiment duration time t. The mean velocity of the fluid was estimated by using a cross correlation technique between the signals obtained for the two tips. The accuracy of the velocity measurements performed under steady flow conditions was estimated at about ±10% for the velocity range analysed (Stutz & Reboud 1997a, b).

The ADV

ADVs have become highly useful in fluid dynamics and are applied to the study of three-dimensional flow and turbulence in both the laboratory and field (rivers, channels and hydraulic structures, amongst others).

The setting characteristics were selected considering that the main objective is to measure the mean velocity and macroscopic turbulence. In this way, the velocity range was selected as ±0.30 m/s with a frequency of 10 Hz, avoiding the noise generated by the equipment when higher frequencies are used. With this setting, the ADV equipment was

able to measure the time-averaged flow field with an accuracy of better than ±0.002 m/s. The kinetic turbulence measured 0.50 m upstream the weir in the experimental facility was used as the inlet condition in the numerical simulations.

EMPIRICAL FORMULAE

Jet parameters

Using instantaneous pressure registers obtained at the bottom of plunge pools, Castillo (2006, 2007) proposed estimators for the nappe flow case: the turbulence intensity at issuance conditions T_u, the jet break-up length L_b, the lateral spread distance ξ, the impingement thickness B_j, and the mean dynamic pressure coefficient C_p.

The turbulence intensity at issuance conditions for laboratory specific flow ($q < 0.25\ m^2/s$) may be estimated as

$$T_u* = q^{0.43}/IC \tag{4}$$

with IC being the initial conditions with dimensions $[L^{0.86}T^{-0.43}]$:

$$IC = 14.95g^{0.50}/\left(K^{1.22}C_d^{0.19}\right) \tag{5}$$

where g is the gravity acceleration, K is a non-dimensional fit coefficient (≈0.85) and C_d is the discharge coefficient $[L^{0.5}T^{-1}]$.

However, for prototype specific flows ($q > > 0.25\ m^2/s$) a mean turbulence index is $T_u \sim 1.2\%$ (Castillo 2006).

The designers need to know the height between the upstream water level and the downstream water level H, the impingement jet thickness B_j, the water cushion depth Y, and the jet break-up length L_b. In this way, the head mean may be calculated at the stagnation point of the plunge pool bottom H_m.

Following the results obtained by Ervine *et al.* (1997) in circular jets, the jet break-up length in the rectangular jet case is calculated as (Castillo 2006)

$$\frac{L_b}{B_i F_i^2} = \frac{K}{\left(K_\varphi T_u F_i^2\right)^{0.82}} \tag{6}$$

with B_i, F_i and $T_u = \overline{V_i'}/V_i$ being the jet thickness, the Froude number and the turbulent intensity at issuance conditions, while K is a non-dimensional fit coefficient (≈ 0.85). $K_\varphi = \overline{V_i'}/w'$ is the turbulent parameter coefficient, where $\overline{V_i'}$ and w' are the root mean square (RMS) and the streamwise turbulent velocity component.

The impingement jet thickness is obtained with the following:

$$B_j = B_g + 2\xi = \frac{q}{\sqrt{2gH}} + 4\varphi\sqrt{h}\left[\sqrt{2H} - 2\sqrt{h}\right] \tag{7}$$

where H is the height between the upstream water level and the downstream water and $\varphi = K_\varphi\ T_u$ is the turbulence parameter in the nappe flow case.

The trajectory of the central nappe may be obtained with the Scimeni (1930) formulation

$$x^* = 2.155(z^* + 1)^{1/2.33} - 1 \tag{8}$$

where $x^* = x/h$ and $z^* = z/h$, with x and z being the coordinate axes considering the origin in the weir crest.

Mean dynamic pressure coefficient

For the mean dynamic pressure coefficient C_p, Castillo (2006) considered two cases (non-effective water cushion and effective water cushion). These formulae have been redefined in this paper considering new laboratory data.

Non-effective water cushion if $Y \leq 5.5B_j$:

when $H/L_b \leq 1.00$:

$$C_p = 1 - 0.0014\, e^{5.755(H/L_b)} \tag{9}$$

when $H/L_b > 1.00$:

$$C_p = 14.643 e^{-3.244(H/L_b)} \tag{10}$$

Effective water cushion if $Y > 5.5B_j$:

$$C_p = \frac{H_m - Y}{V_j^2/2g} = ae^{-b\left(Y/B_j\right)} \tag{11}$$

where H_m is the head mean registered at plunge pool bottom (stagnation point), Y is the depth of the plunge pool and V_j is the impingement velocity. The parameters a and b of Equation (11) may be obtained from Table 2.

Pressure distribution near the stagnation point

There are different formulae for the pressure distribution near the stagnation point of the plunge pool bottom.

Castillo (1989) analysed the results of different authors. b_{distrib} defines the width of the influence region of the pressure (distance between the upstream and downstream points in which the pressure $p = H_m/2$), while y_k is the depth necessary to disintegrate the jet central core in the water cushion. When $b_{\text{distrib}} = 0.13Y$ (Beltaos 1976), Castillo obtained good agreement with the experimental data with Cola (1966) and Hartung & Häusler (1973) formulations. In the last one, the best agreement was obtained with $y_k = 7.2B_j$. For the Aki (1969) formulation, Castillo obtained good agreement by taking into account $b_{\text{distrib}} = 0.23Y$ proposed by Xu & Yu (1983).

In order to know the pressure distribution, the following formula was considered:

$$\frac{p - Y}{H_m - Y} = e^{-\phi'(x/Y)} \tag{12}$$

where p is the mean pressure on the bed of the pool, H_m is the mean pressure at the stagnation point, x is the horizontal distance from the stagnation point to the considered point and Y is the water cushion depth. The parameter ϕ' may be obtained from Table 3. The differences in the results could be due to the diverse working methodologies and experimental conditions.

In a similar way, Bollaert (2002) considers that the longitudinal distribution of the mean dynamic pressure coefficient in circular jets, $C_p(x)$, may be obtained as a function of a non-dimensional radial distance $x/x_{\max}$:

$$\frac{C_p(x)}{C_p} = e^{-K_3(x/x_{\max})^2} \tag{13}$$

where $x_{\max}$ is the maximum longitudinal distance extension of the area influenced by the turbulent shear layer of the impacting jet. This parameter is defined as $x_{\max} = 0.5D_j + 0.25Y$, with D_j being the impingement jet diameter. The value of $0.25Y$ accounts for the spread of the jet through the water depth of the plunge pool (the spread is governed by an outer angle of 13–14°; McKeogh & Elsawy 1980). For the circular jet case, the parameter K_3 ranged from 3 for shallow pool depths to 6 for greater pool depths.

Table 2 | Parameters of the mean dynamic pressure coefficient

H/L_b	a	b
≤0.85	2.50	0.20
0.90–0.99	1.70	0.18
1.00–1.09	1.35	0.18
1.10–1.19	1.05	0.18
1.20–1.29	0.88	0.18
1.30–1.39	0.39	0.15
1.40–1.59	0.24	0.14
≥1.60	0.14	0.12

Table 3 | Parameter of the mean dynamic pressure distribution near the stagnation point (Castillo 1989)

Author	ϕ'	$b_{distrib}$	y_k
Cola (1966)	40.51	$0.13Y$	–
Aki (1969)	12.56	$0.13Y$	–
	12.56	$0.23Y$	–
Hartung & Häusler (1973)	19.60	$0.13Y$	$5B_j$
	40.71	$0.13Y$	$7.2B_j$
Beltaos (1976)	42.01	$0.13Y$	–

NUMERICAL MODELLING

For the numerical modelling, the CFD volume finite scheme program ANSYS CFX has been used. The fluid domain is divided into control volumes, which must satisfy the balance of the governing equations. The code allows different types of elements to be solved. The main difference between the types of elements is the number of nodes used to solve the equations within each control volume. A larger number of nodes per element obtains a more accurate solution in their internal resolution.

In most applications the tetrahedral elements are suitable. However, due to the effect of the take-off of the wall and high turbulence generated in the two-phase (air-water) calculation, the preliminary tests indicated that it would be necessary to use a mesh with hexahedral elements.

All scenarios were obtained by a transient calculation time of 60 s, using 20 Hz frequency, the same as used in the laboratory pressure measurements. The transient statistics were obtained by considering that permanent conditions are reached after 20 s of simulation (Figure 2).

Turbulence models

In order to reach the closure of the Navier–Stokes equations, turbulence models can be used. There are different approximations, from one-equation turbulence models to the direct simulation.

As a compromise between accuracy and computational effort, the RANS turbulence models are widely used. Eddy-viscosity turbulence models consider that such turbulence consists of small eddies which are continuously forming and dissipating, and in which the Reynolds stresses are assumed to be proportional to mean velocity gradients. In this work, some of the most usual RANS turbulence models have been tested for the free falling jet case.

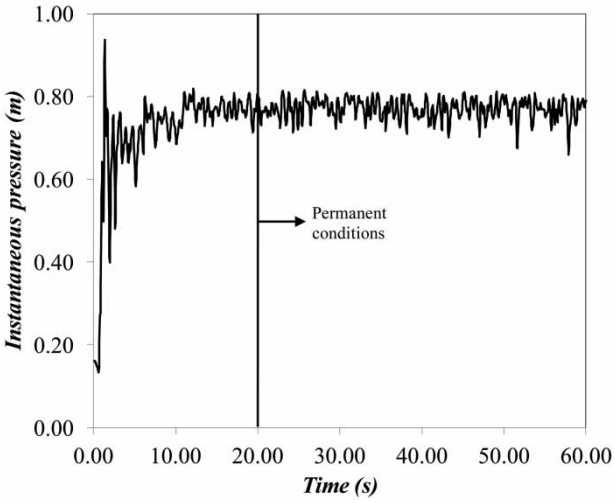

Figure 2 | Transient of pressure at the stagnation point of the plunge pool.

Standard *k-ε* model

This model (Launder & Sharma 1972) is considered as the standard turbulence model and it is considered in the majority of the CFD programs. The effective viscosity is calculated as

$$\mu_t = C_\mu \rho \frac{\kappa^2}{\varepsilon} \tag{14}$$

where C_μ is an empirical coefficient and ε is the dissipation rate of turbulent kinetic energy.

RNG *k-ε* model

In theory, the RNG k-ε model is more accurate than the standard k-ε model. The RNG k-ε turbulence model is based on a renormalisation group analysis of the Navier–Stokes equations. The transport equations for turbulence generation and dissipation are the same as those for the standard model, though the model constants differ and the constant $C_{\varepsilon 1}$ is replaced by the function $C_{\varepsilon 1RNG}$ (Yakhot & Smith 1992).

$$C_{\varepsilon 1RNG} = 1.42 - f_\eta \tag{15}$$

where

$$f_\eta = \frac{\eta\left(1 - \frac{\eta}{4.38}\right)}{(1 + \beta_{RNG}\eta^3)}, \quad \eta = \sqrt{\frac{P_\kappa}{\rho C_{\mu RNG}\varepsilon}} \tag{16}$$

and where $C_{\mu RNG} = 0.085$ is a closure coefficient, β_{RNG} a constant with a value of 0.012, P_k the turbulence production due to viscous forces (ANSYS Inc. 2010), ρ the flow density and ε the dissipation rate of turbulent kinetic energy.

k-ω based SST model

The k-ω turbulence models assume that the turbulence viscosity is linked to the turbulence kinetic energy, k, and the turbulent frequency, ω, as

$$\mu_t = \rho \frac{\kappa}{\omega} \tag{17}$$

The SST model takes into account the accuracy of the k-ω model in the near-wall region and the free stream independence of the k-ε model in the outer part of the boundary layer. To do this, the original k-ω model (Wilcox 2006) is multiplied by a blending function F_1, while the k-ε model (Launder & Sharma 1972) is transformed to a k-ω formulation and multiplied by a function $1–F_1$ (Menter 1994). F_1 is designed to be one inside the boundary layer and decreases to a value of zero away from the surface.

Omega-based baseline Reynolds stress model (BSL)

RSMs are based on transport equations for all components of the Reynolds stress tensor and the dissipation rate. The Reynolds stress transport equations are solved by the individual stress components, instead of using the eddy viscosity hypothesis. This theoretically makes RSMs more suited to complex flows; however, on only a few occasions practice shows that they are superior to two-equation models.

The Reynolds stress-ω turbulence model is based on the ω-equation. In this way, it allows for a more accurate near-wall treatment. Certain authors, such as Wilcox (2006) and ANSYS Inc. (2010), consider the second moment closure turbulence model based on ω as more accurate than that based on k such as the classical Launder *et al.* (1975) model. For this reason, this turbulence model was selected.

Similar to the SST turbulence model, all constants are computed by considering a linear combination from the corresponding constants of the k-ε and the k-ω model. If Φ_1 represents any constant in the original k-ω model and Φ_2 represents any constant in the transformed k-ε model, then the corresponding constant in the model Φ_3 b may be written as

$$\Phi_3 = F_1\Phi_1 + (1 - F_1)\Phi_2 \tag{18}$$

Convergence criteria

In judging the convergence of a solution in a finite-volume scheme, a widely used method entails monitoring the residuals (Wasewar & Vijay Sarathi 2008). Residuals are defined as the imbalance in each conservation equation following each iteration. The solution is said to have converged if the scaled residuals are smaller than prefixed values ranging between 10^{-3} and 10^{-6}. In this work, the residual values were set to 10^{-4} for all the variables.

Free surface modelling

To solve the air-water two-phase flow, the Eulerian-Eulerian multiphase flow homogeneous model was selected. In each control volume, the sum of the volume fraction of all phases (r_α) is the unit. Three conditions are possible for each cell:

- $r_\alpha = 0$. The cell is empty of the α phase.
- $r_\alpha = 1$. The cell is full of the α phase.
- $0 < r_\alpha < 1$. The cell contains the interface between the α phase and one or more other phases.

In general, it may be assumed that the free surface is on the 0.5 air volume fraction. However, due to the high air entrainment in the nappe, the jet thickness and the break-up length were calculated using a 0.8 air volume fraction. The pool depth under nappe was also obtained by considering the ratio 0.8 air volume fraction since the program obtained a huge air entrainment under the nappe. Figure 3 shows the free surface observed in the laboratory device and calculated with CFD methodology when permanent conditions were reached. The jet profiles were very similar.

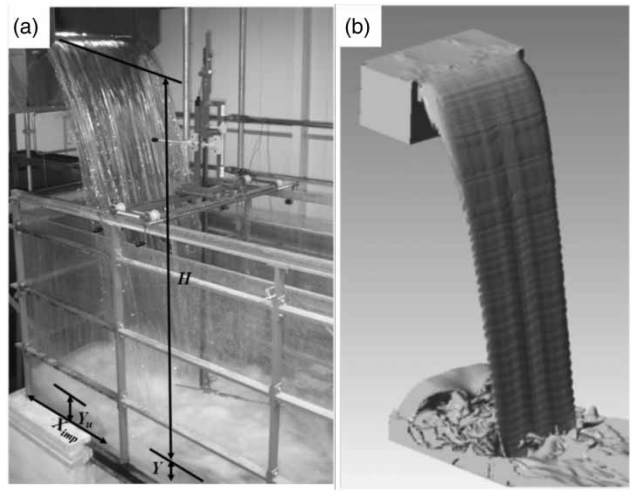

Figure 3 | Free surface of turbulent jets ($q = 0.058$ m^2/s, $H = 2.27$ m, $h = 0.095$ m, $Y = 0.17$ m): (a) structure of turbulent jet; (b) solved with CFD.

Boundary conditions

The model boundary conditions corresponded to the flow, the turbulence at the inlet condition obtained with ADV (located 0.50 m upstream of the weir), the upstream and downstream levels and their hydrostatic pressures distributions (Figure 4).

For simplicity, the symmetry condition in the longitudinal plane of the plunge pool was used.

The inlet condition considers the mass flow rate with a normal direction to the boundary condition ($q = 0.058$ m^2/s, $q = 0.037$ m^2/s, $q = 0.023$ m^2/s), the turbulent kinetic energy (0.00036 m^2/s^2 for $q = 0.058$ m^2/s, 0.00019 m^2/s^2 for $q = 0.037$ m^2/s, 0.00011 m^2/s^2 for $q = 0.023$ m^2/s), and the water level height at upstream deposit (2.445 m for $q = 0.058$ m^2/s, 2.423 m for $q = 0.037$ m^2/s, 2.397 m for $q = 0.023$ m^2/s).

The outlet condition has been considered as an opening condition with flow normal to the boundary condition and hydrostatic pressure. The water level height at outlet has been modified according to the water cushion depth, Y, in the laboratory device.

For the walls of the upper deposit, the weir and the dissipation bowl, no slip wall conditions and smooth walls have been considered.

The atmosphere condition has been simulated as an opening condition with a relative pressure of 0 Pa, air volume fraction of 1 and water volume fraction of 0.

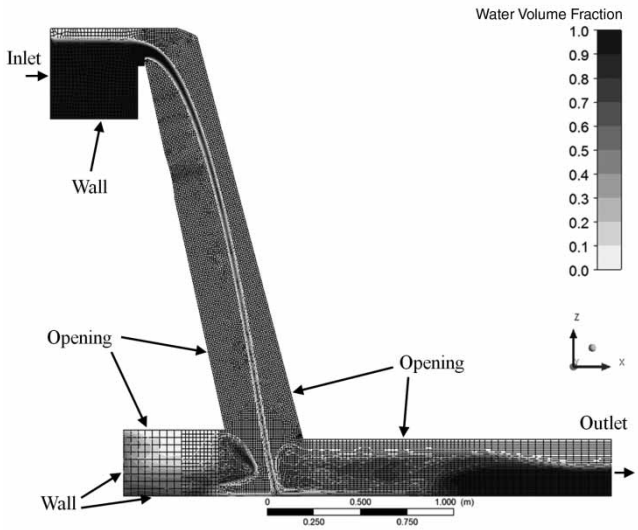

Figure 4 | Scheme of boundary conditions.

RESULTS AND DISCUSSION

Mesh-size analysis

In order to know the effect of the mesh size on the numerical solution of the turbulent jets, a mesh-size analysis was considered. Table 4 shows the total hexahedral elements used in the simulation when different length scales were considered in the falling jet boundary and near the stagnation point.

Following a streamline that starts on the weir, Figure 5 shows the fluid velocity, while Figure 6 indicates the air volume fraction in the falling jet when different mesh sizes were considered. The results are compared with optical fibre measurements.

The mesh size has a small influence on the velocity of the falling jet. The velocity obtained with CFD simulations and optical fibre tended to be slightly smaller than the free-falling velocity due only to the gravity effects. This indicates the effect of air-water friction. To obtain the mean velocity, the optical fibre equipment requires a minimum air entrainment rate in order to obtain a good cross-correlation velocity. In Figure 5, the jet velocity measured is more accurate when the jet is sufficiently aerated. This occurs when the falling height is greater than 1.40 m (velocity greater than 5.30 m/s). At the end of the fall, the numerical simulations and laboratory measurements obtained similar values.

The air volume fraction is highly sensitive to the mesh size. When the mesh size is reduced, results tend to be more accurate. However, smaller elements entail an increment in the computational effort and time required to solve the same problem. In this study, when the mesh size is reduced, good agreement with laboratory data is obtained. Figure 6 shows the comparison of the air volume fraction between optical fibre measurements and CFD. For the two specific flows analysed, the best results were obtained with a mesh size of 0.01 m, approximately half of the free falling jet thickness at the impingement conditions.

Table 4 | Number of elements with regard to the mesh size used

Mesh size (mm)	25.0	15.0	12.5	10.0
Number of elements	48,854	160,308	281,586	456,506

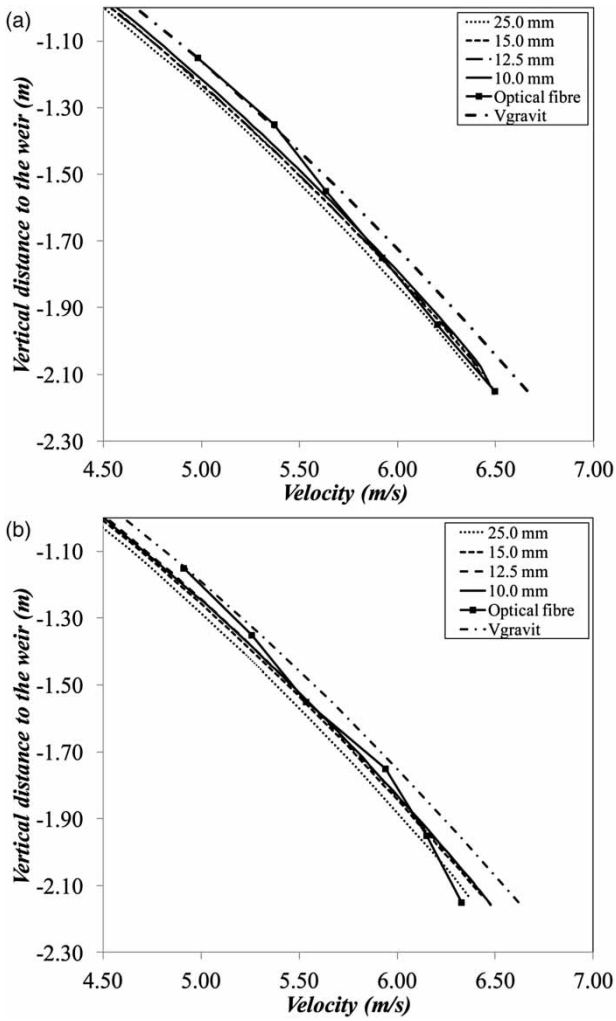

Figure 5 | Flow velocity in the falling jet as a function of the mesh size: (a) $q = 0.058$ m^2/s, $h = 0.095$ m; (b) $q = 0.037$ m^2/s, $h = 0.073$ m.

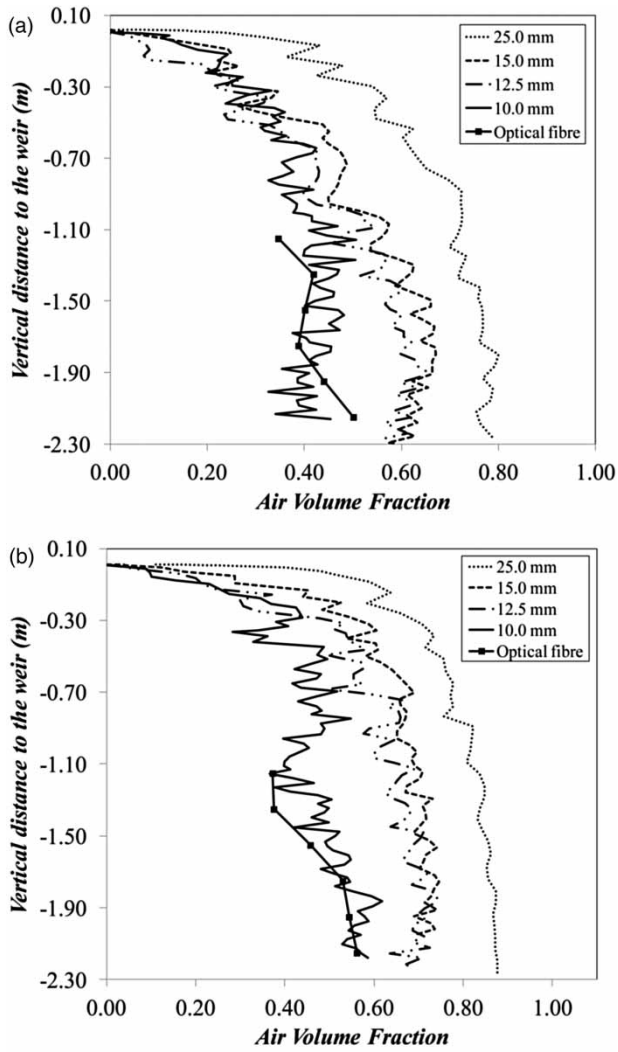

Figure 6 | Air volume fraction in the falling jet as a function of the mesh size: (a) $q = 0.058$ m^2/s, $h = 0.095$ m; (b) $q = 0.037$ m^2/s, $h = 0.073$ m.

Table 5 shows the mean pressure at the stagnation point of the plunge pool for direct impact, when different mesh sizes are considered. Results are in agreement with the air entrainment and the flow velocity simulated during the falling of the jet. Therefore, the best agreement with laboratory results was obtained with a mesh size of 0.01 m. A larger-sized mesh produces lower pressures at the stagnation point due to the jet air entrainment being incorrectly simulated.

Table 5 | Mean pressure at the stagnation point as a function of the mesh size

		Mesh size (mm)			
		25.0	15.0	12.5	10.0
q (m^2/s)	LAB	Mean pressure H_m (m)			
0.058	1.26	0.58	1.03	1.03	1.23
0.037	0.97	0.33	0.69	0.79	1.06

Turbulence in the falling jet

With the aim of knowing the effect of changing the turbulence at the inlet condition of the numerical model in the falling jets, simulations with the RSM turbulent model were carried out by using different turbulences at the inlet condition ($T_u = 0.01$, 0.03, 0.05 and 0.15). Following a streamline, Figure 7 shows the evolution of T_u for each

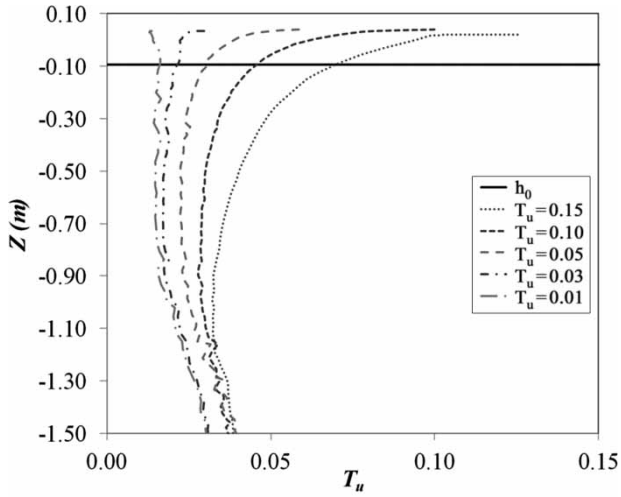

Figure 7 | Evolution of the turbulence of the falling jet.

inlet turbulent intensity when considering a 0.058 m^2/s specific flow. Even though at the inlet condition the turbulences were different, T_u tended to be equal when there were sufficient distances of fall from the weir.

Table 6 indicates the results obtained at the parametric methodology initial conditions ($z = -h$). Although the inlet turbulence had been modified, the mean velocity was not affected. At the initial condition, T_u tended to decrease when the turbulence at the inlet condition was reduced. However, turbulence intensity tended to be a constant value of 0.03 when the fall of the jet increased.

Turbulence models analysis

A comparison of different two-equation turbulence models was also carried out. Considering a mesh size of 0.01 m, the mean computational time was 2.605×10^5 s (≈3.0 days), using a central processing unit (CPU) with two Intel® Xeon® E5620 (Quad Core, 2.40 GHz, 12 MB Cache) processors.

Tables 7 and 8 show a comparison of the most important parameters that appeared in the turbulent jet phenomenon. Data were extracted from the numerical modelling carried out and from measurements observed in the hydraulic laboratory. Data were also compared with the results obtained using the parametric methodology proposed by Castillo (2006), redefined in this work.

Table 7 compares the results obtained with $q =$ 0.058 m^2/s, $H = 2.27$ m and $Y = 0.17$ m. In all of them, an effective water cushion was produced ($Y > 5.5\ B_j$). Besides this, a non-developed jet reached the water cushion, since there was not enough fall distance to produce the disintegration of the jet ($H < L_b$).

Table 6 | Mean velocity and turbulence at issuance condition and after sufficient falling distance as a function of the turbulence at inlet condition ($q = 0.058$ m^2/s, $h = 0.095$ m)

		Issuance condition		z = −1.5 m	
		V (m/s)	T_u (–)	V (m/s)	T_u (–)
T_u at inlet condition (–)	0.15	1.83	0.070	5.50	0.039
	0.10	1.86	0.045	5.52	0.038
	0.05	1.86	0.030	5.52	0.038
	0.03	1.84	0.022	5.50	0.031
	0.01	1.84	0.016	5.50	0.031

Table 7 | Comparison of the principal measurement and calculated variables ($q =$ 0.058 m^2/s, $H = 2.27$ m, $h = 0.095$ m, $Y = 0.17$ m)

	SST	κ-ε	RNG	LAB	PARAM
V_j (m/s)	6.37	6.47	6.59	6.50	6.69
b_j (m)	0.70	0.67	0.69	0.77	–
B_j (m)	0.022	0.022	0.023	–	0.023
L_b (m)	$> H$	$> H$	$> H$	–	2.32
X_{imp} (m)	0.73	0.69	0.73	0.74	0.75
H_m (m)	1.07	1.23	1.25	1.15	1.17
Y_u (m)	0.15	0.15	0.17	0.17	0.18
θ (°)	77.05	78.74	79.21	81	81.37
C_p (–)	0.40	0.47	0.48	0.43	0.44

Table 8 | Comparison of the principal measurement and calculated variables ($q =$ 0.037 m^2/s, $H = 2.30$ m, $h = 0.073$ m, $Y = 0.12$ m)

	SST	κ-ε	RNG	LAB	PARAM
V_j (m/s)	6.27	6.15	6.40	6.33	6.72
b_j (m)	0.64	0.64	0.64	0.67	–
B_j (m)	0.017	0.018	0.017	–	0.017
L_b (m)	$>H$	$>H$	$>H$	–	1.98
X_{imp} (m)	0.63	0.56	0.60	0.64	0.65
H_m (m)	0.71	0.69	0.89	0.81	0.79
Y_u (m)	0.10	0.17	0.17	0.12	0.13
θ (°)	78.33	79.16	79.13	82	82.63
C_p (–)	0.26	0.25	0.34	0.30	0.29

Table 8 shows the results modelled with $q = 0.037$ m^2/s, $H = 2.30$ m and $Y = 0.12$ m, so that an effective cushion is produced ($Y > 5.5\ B_j$). The three turbulence models considered $H < L_b$. Nevertheless, parametric methodology showed that the jet break-up length was reached before the impact ($H > L_b$).

Jet parameters

As far as the falling jet is concerned, CFD simulations followed the jet evolution with good agreement. The jet thickness at impingement conditions was very similar to the parametric methodology when the ratio of 0.8 air volume fraction was considered. With the air–water ratio used, the impingement jet width calculated was a little smaller than that observed in the laboratory. The width of the smaller specific flow was closer than the bigger one, in which the SST turbulence model was more accurate than the other two turbulence models.

In the same way, the velocities obtained at impingement conditions tended to be a little lower than those obtained with an optical fibre equipment, except for that obtained with the RNG k-ε turbulence model that tended to be somewhat larger but smaller than the free-falling velocity. Such velocities match the ratio of head mean at the stagnation point, H_m, between the turbulence models and the laboratory results. The parametric methodology obtains a slightly larger velocity given that the velocity formulation does not include the deceleration through air friction in the falling jet. There are few differences between the impingement jet angles calculated with the turbulence models, which were also similar to the parametric methodology and the laboratory measurements.

Horizontal distance to the stagnation point

For the horizontal distance to the stagnation point, X_{imp}, the results obtained with the SST turbulence model were the most similar to the laboratory and Scimeni (1930) formula, while those obtained through using the k-ε turbulence model were up to 8 cm below laboratory results for the smaller specific flow (between 7% smaller for the higher specific flow and 13% smaller for the smaller specific flow).

Mean dynamic pressure coefficient

For the laboratory measurements and the numerical result, C_p was calculated by using the following expression:

$$C_p = \frac{H_m - Y}{H} \tag{19}$$

For the two specific flows, the energy head, H_m, and the mean dynamic pressure coefficient, C_p, obtained with the three turbulence models were similar to the laboratory measurement and the parametric methodology. In absolute differences, the SST turbulence model was slightly more accurate than the other two turbulence models. SST tended to underestimate the C_P value by 0.03–0.04 (differences of 7–13% with the laboratory result), while the RNG k-ε tended to overestimate it by 0.04–0.05 (differences of 12–13%), and the k-ε model varied between -0.05 to $+0.04$ (9–17%).

Differences between the parametric methodology and laboratory data are about 2–3%.

Ratio between water cushion depth upstream and downstream of the nappe

Water cushion depth under nappe Y_u may be calculated by using the following relation obtained from the momentum equation for the plane jet case (Cui *et al.* 1985) and three-dimensional jet case (Castillo 1989; Castillo & Carrillo 2011)

$$Y_u/Y = \sqrt{1 - 2F_D\left[(V_j/V_D)\beta\cos\theta - 1\right]} \tag{20}$$

where Y is the effective water cushion depth at the plunge pool, $F_D = {V_D}^2/(gY)$ is the square Froude number, V_D is the downstream velocity in the water cushion and θ is the impingement jet angle. β is the head loss coefficient, approximately 0.6 for the plane jet case.

Considering P as the vertical distance from the weir to the bottom of the dissipation basin, Figure 8 shows the laboratory results of $\beta = 0.55$ adjustment for a three-dimensional jet case.

Due to the jet impact and flow recirculation, ANSYS CFX calculated a huge amount of air entrainment in the

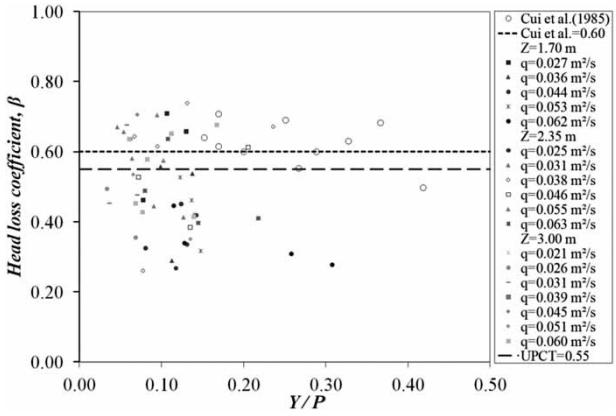

Figure 8 | Head loss coefficient β for the ratio Y/P.

water cushion under the nappe. This made it difficult for the characterisation of the free surface to offer a correct comparison with laboratory measurements and with the Cui *et al.* (1985) studies.

For the higher specific flow, the results of the three turbulence models were very similar to the laboratory data and the empirical formulation. For the smaller specific flow, turbulence models based on the k-ε scheme tended to obtain a greater depth under the nappe (up to 5 cm), while the SST scheme was closer to the laboratory measurements.

Pressure distribution near the stagnation point

The CFD methodology is in agreement with the average pressure distributions near the stagnation obtained in the laboratory when permanent conditions are reached. The three turbulence models obtained similar results upstream and downstream of the stagnation point.

Figure 9 shows the pressure distribution obtained in the laboratory, solved with the CFD program and obtained with classical empirical formulations for two specific flows and effective water cushion depths.

According to the results, the Cola, Aki (when $b_{\text{distrib}} = 0.23Y$), Hartung and Häusler (when $y_k = 7.2B_j$) and Beltaos formulae are equivalent. These formulae are obtained for a non-aerated jet. Their results are in agreement with the data obtained in the laboratory and the numerical simulations with the higher specific flow (case $q = 0.058$ m^2/s, small aeration with $H/L_b = 0.98$).

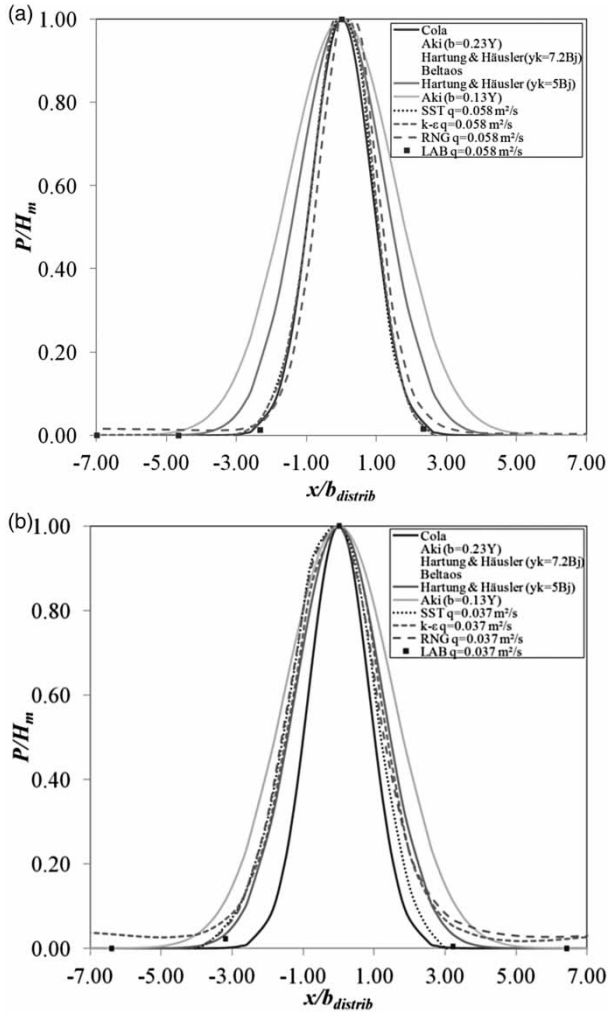

Figure 9 | Pressure distribution near the stagnation point of the plunge pool: (a) $q = 0.058$ m^2/s, $h = 0.095$ m, $H = 2.27$ m, $Y = 0.17$ m; (b) $q = 0.037$ m^2/s, $h = 0.073$ m, $H = 2.30$ m, $Y = 0.12$ m.

The Aki formula with $b_{\text{distrib}} = 0.13Y$ obtains an upper envelope of the mean dynamic pressure distributions proposed by the other authors. As the Aki studies were carried out with aerated jets, the formula is near to an envelope of the laboratory and CFD results for the conditions analysed.

The Hartung and Häusler (when $y_k = 5B_j$) formula obtains results between those proposed by the other authors. Their results match with the laboratory and numerical values obtained for the smaller specific flow (case $q = 0.037$ m^2/s, intermediate aeration with $H/L_b = 1.16$).

In both cases, the best agreement of the numerical simulation has been obtained with the SST turbulence model.

For the higher specific flow, the three turbulence models show similar results. For the smaller specific flow, the k-ε turbulence model tends to overestimate the pressure upstream of the stagnation point, while downstream of the stagnation point the k-ε and RNG turbulence models overestimate the laboratory results.

Figure 10 shows the mean dynamic pressure distribution considering the Bollaert (2002) exponential formula as a function of a non-dimensional radial distance $x/x_{\max}$. Two specific flows and effective water cushion depths have been considered.

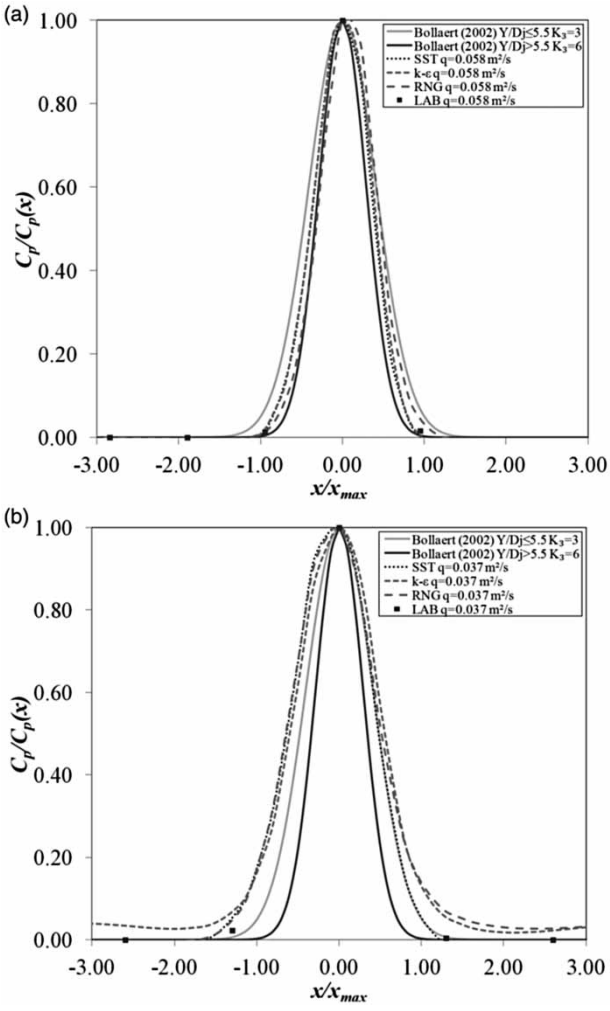

Figure 10 | Pressure distribution near the stagnation point of the plunge pool as a relation of the distance to maximum longitudinal distance: (a) $q = 0.058$ m^2/s, $h = 0.095$ m, $H = 2.27$ m, $Y = 0.17$ m; (b) $q = 0.037$ m^2/s, $h = 0.073$ m, $H = 2.30$ m, $Y = 0.12$ m.

In both cases, a non-symmetrical distribution upstream and downstream of the stagnation point has been obtained by the numerical simulations (more clearly in the smaller specific flow). This matches with the expected behaviour in overflow nappe impingement jets, where the upstream pressure distribution tends to be a bit bigger.

When there are depth pool water conditions, the Bollaert distribution, obtained for circular jet and valid for $H/L_b \leq 0.5$, considers the parameter $K_3 = 6$. This distribution is in agreement with the results obtained by the numerical simulations and laboratory data when the small aerated case ($q = 0.058$ m^2/s, $H/L_b = 0.98$) is considered (Figure 10).

When the jet is more aerated ($q = 0.037$ m^2/s, $H/L_b = 1.16$), the Bollaert assumptions work as smaller envelopes of the pressure distribution. These values can be represented by using $K_3 = 1.5$, instead of $K_3 = 3$ or $K_3 = 6$ suggested in circular jets for shallow pool depths or for greater pool depth conditions, respectively.

Upstream, the SST and RNG numerical results are a bit smaller than laboratory data, while the k-ε turbulence model tends to overestimate the pressure. Downstream of the stagnation point, the k-ε and RNG turbulence models overestimate the laboratory results.

Systematic study

Once the different results had been obtained and analysed, a systematic study of three different specific flows (0.023, 0.037 and 0.058 m^2/s) and four water cushions was carried out (one non-effective and three effective water cushion depths). Simulations were launched by using a mesh size of 0.01 m based on hexahedral elements and SST turbulence model. Results were compared with laboratory measurements and parametric methodology. Table 9 collects the results obtained at the stagnation point.

In general, good agreement was obtained for the mean pressure coefficients and the head mean with the three methodologies. Maximum differences among laboratory, parametric methodology and numerical results corresponded with direct impacts. In these cases, the pass from kinetic energy to potential energy is very abrupt, with significant pressure gradients appearing in reduced areas.

Considering the height between upstream water level and downstream water level, H, of each test, differences

Table 9 | Results obtained at the stagnation point

			CFD		LAB		PARAM	
q (m^2/s)	Y (m)	H (m)	H_m (m)	C_p (–)	H_m (m)	C_p (–)	H_m (m)	C_p (–)
0.023	0.02	2.377	0.36	0.14	0.41	0.16	0.45	0.18
0.023	0.11	2.277	0.35	0.10	0.34	0.10	0.35	0.11
0.023	0.22	2.177	0.22	0.00	0.29	0.03	0.29	0.03
0.023	0.30	2.097	0.30	0.00	0.31	0.00	0.32	0.01
0.037	0.02	2.397	1.06	0.45	0.97	0.39	0.70	0.28
0.037	0.12	2.297	0.71	0.26	0.81	0.30	0.79	0.29
0.037	0.24	2.177	0.44	0.09	0.43	0.08	0.44	0.09
0.037	0.33	2.087	0.32	0.00	0.39	0.03	0.41	0.04
0.058	0.03	2.411	1.23	0.46	1.26	0.51	1.24	0.50
0.058	0.17	2.276	1.07	0.40	1.15	0.43	1.17	0.44
0.058	0.25	2.191	0.88	0.29	0.73	0.22	0.78	0.24
0.058	0.35	2.091	0.56	0.10	0.55	0.10	0.57	0.11

between simulations and laboratory data show a maximum error from −4 to 7%.

In these cases of direct impact, laboratory results revealed that the C_p is very sensitive to the H/L_b rate when H/L_b is between 0.70 and 1.30.

CONCLUSIONS

In general, the results obtained with ANSYS CFX offered good agreement with the laboratory measurements and the parametric methodology. However, given that RANS turbulence models were used, the program obtained an average pressure register in contrast to the natural variability of the phenomenon which limited the possible analysis of fluctuant dynamic pressures.

The jet velocity obtained with CFD and optical fibre showed the effect of air-water friction during the falling. Whereas the mesh size had a small influence in the falling jet velocity, the air volume fraction was highly sensitive to the mesh size.

Mean pressure at the stagnation point was in agreement with the air entrainment and flow velocity of the jet. The best agreement with laboratory results was obtained with a mesh size approximately half of the free falling jet thickness at the impingement conditions. A larger-sized mesh produced lower pressures at the stagnation point due to the jet air entrainment being incorrectly simulated.

With the mesh size used, the homogeneous Eulerian two-phase model did not allow monitoring of the formation of the drops in the free surface of the falling jet. Consequently, it was difficult to interpret the results of the jet break-up length and different scale effects. Even though at the inlet condition the turbulences were different, T_u tended to be equal when there were sufficient distances of fall from the weir when using a second moment closure turbulent model.

As far as the turbulence models comparison is concerned, there was little variation among the turbulence models used in the study. The SST turbulence model obtained results slightly similar to those found in the laboratory and with parametric methodology. ANSYS CFX calculated a significant amount of air entrainment in the water cushion under the nappe. This made it difficult to characterise the water depth in this region.

In both pressure distributions near the stagnation point cases, the classical formulae and the Bollaert one, the SST turbulence model seems to be the most accurate. For the smaller specific flow, the k-ε tended to overestimate the pressure distribution upstream and downstream, while the RNG tended to overestimate downstream.

Using the SST turbulence model, good agreement was obtained for the mean pressure coefficients and the head

mean with laboratory results and parametric methodology. Considering the height between the upstream water level and downstream water level of each test, differences between simulations and laboratory data showed a maximum error from −4 to 7%.

With the aim of improving the design of overtopping flows and their energy dissipation, it would be necessary to provide advances in the knowledge and characteristics of the hydrodynamic actions. More experimental studies, both in physical models and prototypes, are necessary in characterising simultaneously the phenomena produced in the jets (aeration and velocity), combined with measurements of pressures, velocities and aeration rates in stilling basins.

In order to develop this work further, the researchers plan to examine use of inhomogeneous models and hence identify results independent from the mesh size. In future activities, velocities and air entrainment in the stilling basin will be analysed by using different turbulence models. Comparison with diverse CFD codes (open source and commercial ones) will be considered.

ACKNOWLEDGEMENTS

The researchers express their gratitude for the financial aid received from the Ministerio de Economía y Competitividad and the Fondo Europeo de Desarrollo Regional (FEDER) through the Natural Aeration of Dam Overtopping Free Jet Flows and its Diffusion on Dissipation Energy Basins project (BIA2011-28756-C03-02). The authors are also grateful to the editors and the three anonymous reviewers for their constructive comments that helped us to improve the quality and clarity of the paper.

REFERENCES

Aki, S. 1969 Study on fluctuating characteristics of water dynamic force acting on base of free overfall. CRIEPI Research Report No. 69009 (in Japanese).

Annandale, G. W. 2006 *Scour Technology. Mechanics and Engineering Practice*. McGraw-Hill, New York.

ANSYS, Inc. 2010 ANSYS CFX. Solver Theory Guide. Release 13.0.

Asadollahi, P., Tonon, F., Federspiel, M. P. E. A. & Schleiss, A. J. 2011 Prediction of rock block stability and scour depth in plunge pools. *J. Hydraul. Res.* **49** (6), 750–756.

Azamathulla, H. M., Ghani, A. A. & Zakaria, N. A. 2009 ANFIS based approach for predicting maximum scour location of spillway. *Water Manage. ICE London* **162** (6), 399–407.

Azis, T. N., Raiford, J. P. & Khan, A. A. 2008 Numerical simulation of turbulent jets. *Eng. Appl. Comp. Fluid Mech.* **2** (2), 234–243.

Balabel, A., Hegab, A., Nasr, M. & El-Behery, S. 2011 Assessment of turbulence modeling for gas flow in two-dimensional convergent–divergent rocket nozzle. *Applied Mathematical Modelling* **35**, 3408–3422.

Beltaos, S. 1976 Oblique impingement of circular turbulent jets *J. Hydraul. Res.* **14** (1), 17–36.

Boes, R. & Hager, W. H. 1998 Fiber-optical experimentation in two-phase cascade flow. In: *Proceedings of the International RCC Dams Seminar* (K. Hansen, ed.). CD. Denver, USA.

Bollaert, E. F. R. 2002 Communication 13. Transient water pressures in joints and formation of rock scour due to high-velocity jet impact. In: *Laboratoire de Constructions Hydrauliques* (A. J. Schleiss, ed.). École Polytechnique Fédérale de Lausanne, Lausanne.

Bollaert, E. F. R. & Schleiss, A. 2003 Scour of rock due to the impact of plunging high velocity jets part I: a state-of the-art review. *J. Hydraul. Res.* **41** (5), 451–464.

Castillo, L. 1989 Metodología experimental y numérica para la caracterización del campo de presiones en los disipadores de energía hidráulica. Aplicación al vertido libre en presas bóveda. PhD Thesis. Departamento de Ingeniería Hidráulica, Marítima y Ambiental. Universitat Politècnica de Catalunya, Barcelona (in Spanish).

Castillo, L. 2006 Aerated jets and pressure fluctuation in plunge pools. In: *Proceedings of the 7th International Conference on Hydroscience and Engineering*. Philadelphia, USA, pp. 1–23.

Castillo, L. 2007 Pressure characterisation of undeveloped and developed jets in shallow and deep pool. In: *Proceedings of the 32nd IAHR Congress*. 1 July–6 July 2007, Venice, Italy, pp. 645–655.

Castillo, L. & Carrillo, J. M. 2011 Numerical simulation and validation of hydrodynamics actions in energy dissipation devices. In: *Proceedings of the 34th IAHR World Congress*. 26 June–1 July 2011, Brisbane, Australia, pp. 4416–4423.

Castillo, L. & Carrillo, J. M. 2012 Hydrodynamics characterisation in plunge pools. Simulation with CFD methodology and validation with experimental measurements. In: *Proceedings of the 2nd European IAHR Congress*. 27 June–29 June 2012, Munich, Germany.

Castillo, L. & Carrillo, J. M. 2013 Analysis of the scale ratio in nappe flow case by means of CFD numerical simulation. In: *Proceedings of the 2013 IAHR Congress.* 8 September–13 September 2013, Chengdu, China.

Castillo, L., Puertas, J. & Dolz, J. 2007 Discussion of 'Scour of rock due to the impact of plunging high velocity jets. Part I: a

state-of-the-art review' by E.F.R. Bollaert and A.J. Schleiss. *J. Hydraul. Res.* **45** (6), 853–858.

Chau, K. W. & Jiang, Y. W. 2001 3D numerical model for Pearl River estuary. *J. Hydraul. Eng., ASCE* **127** (1), 72–82.

Chau, K. W. & Jiang, Y. W. 2004 A three-dimensional pollutant transport model in orthogonal curvilinear and sigma coordinate system for Pearl River estuary. *Int. J. Environ. Pollut.* **21** (2), 188–198.

Cola, R. 1966 Diffusione di un getto piano verticale in un bacino d'acqua d'altezza limitata. *L'energia Elettrica* **11**, 649–664 (in Italian).

Cui, G. T., Lin, J. Y. & Liang, X. R. 1985 Study on the force and effect of the arch dam overflow water tongue on the river bed. *J. Hydraul. Eng. Beijing* **8**, 53–68 (in Chinese).

Davies, J. T. 1972 *Turbulence Phenomena*. Academic Press, New York and London.

Ervine, D. A., Falvey, H. T. & Withers, W. A. 1997 Pressure fluctuations on plunge pool floors. *J. Hydraul. Res.* **35** (2), 257–279.

Federspiel, M. P. E. A. 2011 Response of an Embedded Block Impacted by High-velocity Jets. PhD Thesis. Faculté environnement naturel, architectural et construit. École Politechnique Fédérale de Lausanne, Lausanne.

Guha, A., Barron, R. M. & Balachandar, R. 2010 Numerical simulation of high-speed turbulent water jets in air. *J. Hydraul. Res.* **48** (1), 119–124.

Hartung, F. & Häusler, E. 1973 Scours, stilling basins and downstream protection under free overfall jets at dams. In: *Proceedings of the 11th Congress on Large Dams*. Madrid, Spain, pp. 39–56.

Haun, S., Olsen, N. R. B. & Feurich, R. 2011 Numerical modeling of flow over trapezoidal broad-crested weir. *Eng. Appl. Comp. Fluid Mech.* **5** (3), 397–405.

Ho, D. K. H. & Riddette, K. M. 2010 Application of computational fluid dynamics to evaluate hydraulic performance of spillways in Australia. *Aust. J. Civil Eng.* **6** (1), 81–104.

Horeni, P. 1956 Disintegration of a free jet of water in air. Byzkumny ustav vodohospodarsky prace a studie, Sesit 93, Praha, Pokbaba (in Czech).

Lai, W. & Khan, A. A. 2012 Discontinuous Galerkin method for 1D shallow water flows in natural rivers. *Eng. Appl. Comp. Fluid Mech.* **6** (1), 74–86.

Launder, B. E. & Sharma, B. I. 1972 Application of the energy dissipation model of turbulence to the calculation of flow near a spinning disc. *Lett. Heat Mass Transfer* **1** (2), 131–138.

Launder, B. E., Reece, G. J. & Rodi, W. 1975 Progress in the development of a Reynolds-stress turbulence closure. *J. Fluid Mech.* **68** (3), 537–566.

Mahmoud, H., Kriaa, W., Mhiri, H., Le Palec, G. & Bournot, P. 2012 Numerical analysis of recirculation bubble sizes of turbulent co-flowing jet. *Eng. Appl. Comp. Fluid Mech.* **6** (1), 58–73.

McKeogh, E. J. & Elsawy, E. M. 1980 Air retained in pool by plunging water jet. *J. Hydraul. Div.* **106** (10), 1577–1593.

Melo, J. F., Pinheiro, A. N. & Ramos, C. M. 2005 Forces on plunge pool slabs: influence of joints location and width. *J. Hydraul. Eng.* **132** (1), 49–60.

Menter, F. R. 1994 Two-equation eddy-viscosity turbulence models for engineering applications. *AIAA J.* **32** (8), 1598–1605.

Moore, W. L. 1943 Energy loss at the base of a free overfall. *Trans. Am. Soc. Civil Eng.* **108** (1), 1343–1360.

Puertas, J. 1994 Criterios hidráulicos para el diseño de cuencos de disipación de energía en presas bóveda con vertido libre por coronación. PhD Thesis. Departamento de Ingeniería Hidráulica, Marítima y Ambiental. Universitat Politècnica de Catalunya, Barcelona (in Spanish).

Rahimzadeh, H., Maghsoodi, R., Sarkardeh, H. & Tavakkol, S. 2012 Simulating flow over circular spillways by using different turbulence models. *Eng. Appl. Comp. Fluid Mech.* **6** (1), 100–109.

Scimeni, E. 1930 Sulla forma delle vene tracimanti. *ÍEnergia Elettrica* **7** (4), 293–305 (in Italian).

Stutz, B. & Reboud, J. L. 1997a Experiment on unsteady cavitation. *Exp. Fluids* **22** (1997), 191–198.

Stutz, B. & Reboud, J. L. 1997b Two-phase flow structure of sheet cavitation. *Phys. Fluids* **9** (12), 3678–3686.

Wahl, T. L., Frisell, K. H. & Cohen, E. A. 2008 Computing the trajectory of free jets. *J. Hydraul. Eng.* **134** (2), 256–260.

Wasewar, L. & Vijay Sarathi, J. 2008 CFD modelling and simulation of jet mixed tanks. *Eng. Appl. Comp. Fluid Mech.* **2** (2), 155–171.

Wilcox, D. C. 2006 *Turbulence Modeling for CFD*, 3rd edn. DCW Industries, Inc., La Canada, California.

Wu, C. L. & Chau, K. W. 2006 Mathematical model of water quality rehabilitation with rainwater utilisation – a case study at Haigang. *Int. J. Environ. Pollut.* **28** (3–4), 534–545.

Xu, D. M. & Yu, C. Z. 1983 Pressures on the bottom of a channel due to the impact of a plane jet and their fluctuant characteristics. *Shuili xuebao, Beijin* **5**, 52–58 (in Chinese).

Yakhot, V. & Smith, L. M. 1992 The renormalisation group, the ε-expansion and derivation of turbulence models. *J. Sci. Comput.* **7** (1), 35–61.

First received 1 October 2013; accepted in revised form 18 December 2013. Available online 18 January 2014